CHALMERS
UNIVERSITY OF TECHNOLOGY

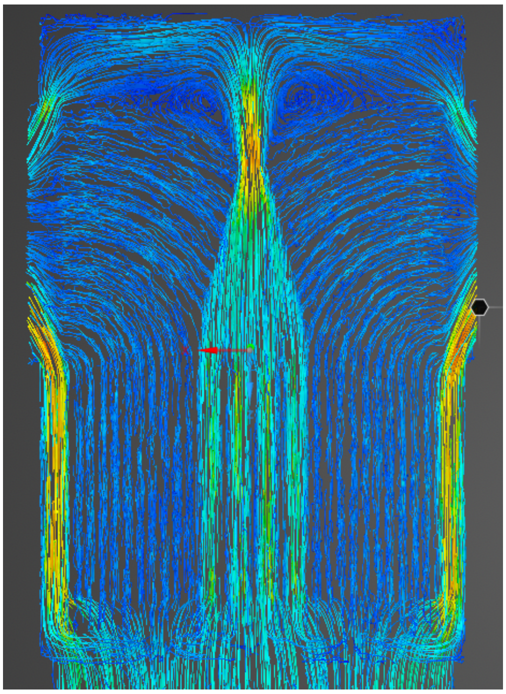

Influence of outlet geometry on cooling and pressure drop in a 5G radio device

An experimental and CFD study on the pressure drop and heat transfer associated with forced air flow through a 5G remote radio device at Ericsson AB

Master's thesis in Sustainable Energy Systems

Mohammed Mubeen Shaikh

DEPARTMENT OF MECHANICS AND MARITIME SCIENCES
CHALMERS UNIVERSITY OF TECHNOLOGY
Gothenburg, Sweden 2022
www.chalmers.se

Master's thesis 2022

Influence of outlet geometry on cooling and pressure drop in a 5G radio device

An experimental and CFD study on the pressure drop and heat transfer associated with forced air flow through a 5G remote radio device at Ericsson AB

MOHAMMED MUBEEN SHAIKH

Department of Mechanics and Maritime Sciences
Division of Fluid dynamics
Chalmers University of Technology
Gothenburg, Sweden 2022

Influence of outlet geometry on cooling and pressure drop in a 5G radio device
An experimental and CFD study on the pressure drop and heat transfer associated with forced air flow through a 5G remote radio device at Ericsson AB
MOHAMMED MUBEEN SHAIKH

Supervisor: Stefan Skoglund, Thermal Design team, Ericsson AB
Examiner: Tomas Grönstedt, Department of Mechanics and Maritime Sciences

Master's Thesis 2022
Department of Mechanics and Maritime Sciences
Division of Fluid dynaics
Chalmers University of Technology
SE-412 96 Gothenburg
Telephone +46 31 772 1000

Cover: Simulation of internal flow through the radio device studied on ANSYS Discovery$^{\mathrm{TM}}$, showing streamlines of velocity.

Typeset in LaTeX
Printed by Chalmers Reproservice
Gothenburg, Sweden 2022

Influence of outlet geometry on cooling and pressure drop in a 5G radio device
An experimental and CFD study on the pressure drop and heat transfer associated with forced air flow through a 5G remote radio device at Ericsson AB
MOHAMMED MUBEEN SHAIKH,
Department of Mechanics and Maritime Sciences
Chalmers University of Technology

Abstract

With the rapid increase in the number of 5G users every year, the demand for increased connectivity and reduced lag time is consequently rising. An accelerated growth in the number of 5G radio devices is expected and along with it, the energy requirements of said devices is also expected to sharply rise. It is vital that the cooling and ventilation in these radio devices is optimized to ensure maximum efficiency. In this study, the effect of the outlet geometry of radio devices on the overall internal ventilation and the associated cooling is observed. Four outlet geometries (Hexagonal, Louvers, Tall stripes, Uni-gill) are studied both experimentally and by steady-state Computational Fluid Dynamics (CFD) simulations at Ericsson AB.

The experimental tests were performed to simulate the heat generation within the radio device and a wind tunnel was used to mock the air flow within it. The hexagonal outlet shape proved to have required a lower pressure drop and hence lower fan power requirement as compared to the Louvers outlet shape. Better heat sink temperature distribution was also observed on the hexagonal outlet shape.

Having conducted the CFD simulations, it was understood that the outlet geometries that resulted in higher Reynolds numbers in the heat sink produced lower pressure drops and better cooling. A Nusselt number correlation was also used to validate the heat transfer in the Heat Sink ducts and the calculated values agree with the literature. The production of acoustical noise with the hole patterns was not explicitly studied but was observed during the experimental tests and holds a scope for future studies.

Keywords: 5G radio, CFD, heat sink tests, outlet geometry, Nusselt number, internal flow.

Acknowledgements

This thesis project has turned out to be a fantastic learning experience for me. I would like to thank my supervisor at Ericsson AB, Stefan Skoglund for providing me with this opportunity and for being a reliable mentor. My heartfelt gratitude to my CFD advisor at Ericsson, Achref Rabhi, for his continued support and encouragement, this work has been significantly improved from his advice. I would also like to thank my thesis examiner, Tomas Grönstedt for giving me timely advice and being a compassionate professor. I was also supported by Joakim Bonilla at Ericsson with the design of the radio device, which I am very thankful for. I would like to thank the staff from the thermal design team at Ericsson, Kista for helping with setting up the experiments and providing much needed tips to improve the test quality. My thanks to all my professors during my education for being patient with me, and providing me immense inspiration to study and ask more questions. I am grateful to having had the opportunity to pursue a higher education at Chalmers University, a nurturing environment like no other. Finally, I would like to thank my family and my dear friends for being my support system and constantly motivating me to be a better person.

Mohammed Mubeen Shaikh, Gothenburg, August 2022

List of Acronyms

Below is the list of acronyms that have been used throughout this thesis listed in alphabetical order:

5G	5^{th} Generation
CAD	Computer Aided Design
CFD	Computational Fluid Dynamics
FDM	Finite Difference Method
FEM	Finite Element Method
FVM	Finite Volume Method
HS	Heat Sink
HVAC	Heating, Ventilation and Air Conditioning
IP	Internet Protocol
LFE	Laminar Flow Element
OP	Operating Point
PCB	Printed Circuit Board
PLA	Poly Lactic Acid
RD	Radio Device
RF	Radio Frequency

Nomenclature

Below is the nomenclature of variables and symbols that have been used throughout this thesis.

P	Static pressure
P_0	Total pressure
ρ	Density
v	Fluid velocity
τ	Stress tensor
μ	Molecular viscosity, Dynamic viscosity
E	Total energy
h	Sensible enthalpy, Convective heat transfer coefficient
k	Thermal conductivity, Turbulent kinetic energy
k_t	Turbulent thermal conductivity
ω	Turbulent dissipation rate
G_k^*	Turbulent kinetic energy generation
G_ω	Turbulent dissipation rate generation
Γ_k	Effective diffusivity of turbulent kinetic energy
Γ_ω	Effective diffusivity of turbulent dissipation rate
Y_k	Turbulent kinetic energy dissipation
Y_ω	Turbulent dissipation rate dissipation
d_h	Hydraulic diameter
Re	Reynolds number
T_s	Solid surface temperature
$T(r, 0)$	Free stream temperature
δ_t	Boundary layer thickness
$q"_s$	Heat flux
Nu	Nusselt number
Pr	Prandtl number

Contents

List of Figures

List of Tables

1

Introduction

The world of wireless mobile communication networks is expanding every year and is crucial to most of the integrated technology services used today. Considering that the transition from one generation of wireless network to another occurs approximately once in every decade [1], it is crucial that the optimization and the maturation for each generation occurs in due time.

At present, the 5th Generation (5G) of mobile network systems is being implemented, with 660 Million subscriptions across the globe [2]. The increased network connectivity and faster data transfer rates will allow 5G systems to facilitate newer technologies like Internet of Things, Cognitive Radio Networks, and a pantheon of cloud-based operations [3]. That said, it is also necessary to keep in mind the linked side-effects of a rapidly increasing Internet Protocol (IP) traffic, which has increased 3-fold from 2017 to 2022 [4].

This is also in correlation with previous studies which predict that the energy consumption on the mobile operator end, and data center ends will see a sharp increase with the coming years [5]. It has been predicted that the mobile network architecture will observe a 5% increase per annum on the annual energy consumption. A major portion of this energy consumption is attributed to the HVAC systems within the radio devices which are a crucial part of the mobile network architecture.

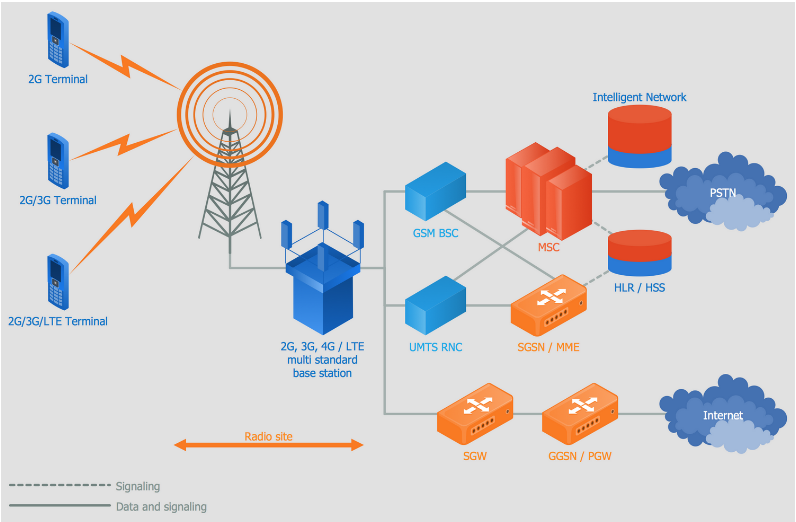

Figure 1.1: Illustration of a typical mobile network architecture

.

A typical mobile network architecture scheme can be observed from Figure 1.1[1]. One can observe a base station from the illustration, which is a crucial component in any mobile network architecture. A base station is a comprehensive structure whose primary function is to produce and transmit radio signals at different frequencies according to the network demands. It is equipped with a number of RDs to achieve the said function.

Modern RDs aim at reducing their energy demands by promoting both active and passive cooling [7]. To ameliorate active cooling of radio devices, functions such as deep sleep [7] which are programmed to hibernate the radio devices during periods of low usage, are programmed. Along with these programmed functions, it is also necessary that all the parts of the HVAC system within these RDs are optimized for minimum energy consumption.

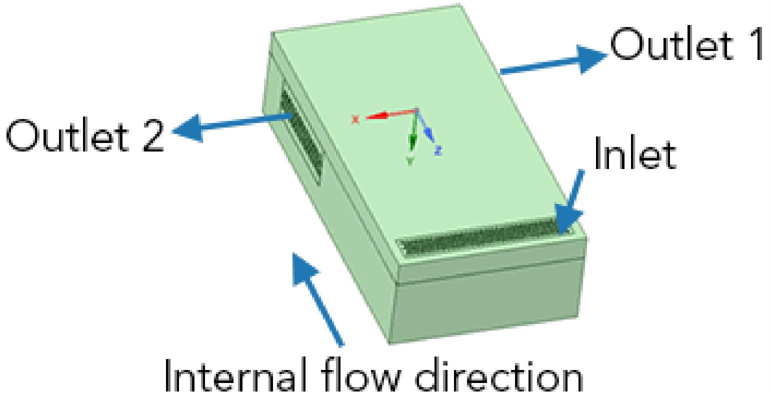

Figure 1.2: A generic design for a radio device, emphasizing the direction of the air flow through it.

A general design of the RD in focus in this study can be seen in Figure 1.2. The goal of this study is to analyze the impact of the outlet geometry on the internal flow within these RDs and how the cooling of these devices is affected.

1.1 Need for current study

For the purpose of inspiration several pieces of literature were referred to, during this study. Untaroiu et al. [8], studied the geometrical shape of hole patterns in turbo-machinery seals to reduce leakage between seals. CFD data along with certain design of experiment techniques revealed a relationship between the amount of fluid

---

[1] Source: [6]

leakage and certain geometric parameters such as hole diameter, depth, spacing etc. Nielsen et al. [9], studied the rotor dynamic forces experienced by the previously mentioned seals due to the bulk flow. Once again, a variety of hole patterns were studied, and analyzed by comparing CFD calculations with experimental data.

The aforementioned studies provide substantial insight into optimization techniques for rotordynamic forces and implementation of experimental data for CFD validation.

In the realm of electronics cooling, Boukhanouf and Haddad [10] studied the usage of vapour chambers to reduce the operating temperatures of RF components using CFD analysis. This study provides good insight into heat dissipation of RF components and their related temperature tolerances. Leung and Kang [11] experimentally study the laminar convection within vertical and horizontal PCB assemblies. A relationship between the dimensions of the electronic components, the Reynolds number and the heat transfer coefficient was observed.

The above mentioned studies also relate the cooling within electronic assemblies to the flow rate of the air, pressure drop inside the assemblies etc. But from [9, 8] it is also evident that geometry also affects the fluid flow. There is a dearth of information regarding the influence of geometry, or outlet geometry on the cooling within electronic assemblies. This represents a gap in the current realm of research and this study aims at reducing this gap by:

- Experimentally carrying out tests and measuring the performance of different outlet patterns on the basis of temperature distribution on the HS.
- Conducting experimental tests and then CFD simulations to validate the test results.
- Using theoretical knowledge to understand the nature of cooling performance and pressure drops in different tests. Additionally, plotting the results from these tests to observe a trend in the results.

2

Theory

2.1 Pressure drop - static, dynamic, total pressure

One of the most useful equations to studying fluid dynamics is the Bernoulli's equation. It lays the groundwork in coupling the influence of flow velocity to the total pressure of the fluid and is also crucial in interpreting a number of results obtained during the course of this project. For an incompressible, inviscid flow, having very little or no changes in relative elevation of the fluid flow, Bernoulli's equation can be expressed as [12]:

$$P + \frac{1}{2}\rho v^2 = P_0 \tag{2.1}$$

Where, P is the static pressure of the fluid measured at a point, $\frac{1}{2}\rho v^2$ is the dynamic pressure of the fluid, with ρ being the density of the fluid and v being the velocity of the fluid and P_0 is the total pressure or the stagnation pressure of the fluid.
During the lab tests, the measured pressure is very close to the the stagnation pressure of air. This is owing to the density of the air at room temperature, and the very low inlet velocities.

2.2 The conservation equations

To provide the reader a brief introduction to CFD, it is crucial that the equations and the mathematical models that are solved in the CFD problem in focus are glanced over. This section also aims at providing a brief overview of the continuity equations used in the CFD simulation software used for this study, ANSYS Fluent$^{\text{TM}}$ 2021 R2.
To begin with, CFD is a branch of computational physics and mathematics that is associated with the modeling of a fluid flow phenomenon within a certain physical domain. The general practice for solving a CFD problem involves FVM to discretize the physical governing equations. FVM is a robust tool for the numerical representation of fluid flow problems and heat transfer, within an acceptable margin of error. Additionally, in fluid simulations with an unstructured mesh and relatively simple physical phenomena, FVM is more efficient compared to other methods such as FDM or FEM
It requires that the domain is segregated into a number of small volumes. Following which, surface integrals of the vector fields are obtained using the divergence theorem. This calculated flux is further discretized at the surfaces of volumes for the

discrete unknowns involved [13].
The main conservation equations solved in ANSYS Fluent$^{\text{TM}}$ for problems involving incompressible fluid flow and heat transfer are:

1. Mass conservation equations
2. Momentum conservation equations
3. Energy conservation equations

2.2.1 Mass conservation law

This section pertains to the conservation of mass within the fluid domain i.e, the mass entering the volume is equal to the mass leaving it. This conservation in a steady state, incompressible flow problem can be numerically expressed as:

$$\nabla.(\vec{v}) = 0 \tag{2.2}$$

2.2.2 Momentum conservation law

This section pertains to the numerical modeling of the conservation of momentum within the domain. To begin with, the law of conservation of momentum states that the total momentum within the system is conserved, i.e, there is no generation of momentum within the system, it is only transferred between media. For a steady state, incompressible flow problem this is numerically modeled on ANSYS Fluent$^{\text{TM}}$ as [14]:

$$\nabla.(\vec{v}\vec{v}) = -\nabla p + \nabla.(\tau) + \rho\vec{g} + \vec{F} \tag{2.3}$$

where τ is the stress tensor which can be represented as[14]:

$$\tau = \mu\Big[(\nabla\vec{v} + \nabla\vec{v}^T) - \frac{2}{3}\nabla.\vec{v}I\Big] \tag{2.4}$$

where μ is the molecular viscosity and I is the unit tensor. The second term on the right hand side represents the effect of volume dilation in the domain. $\rho\vec{g}$ and $\vec{F}$ are the gravitational force and the body force respectively.

2.2.3 Energy conservation law

The problem under focus involves both conduction and convection. For this purpose, the energy equation solved is represented as:

$$\nabla.(\vec{v}(\rho E + p)) = \nabla.\Big(k_{eff}\nabla T + (\tau_{eff}.\vec{v})\Big) \tag{2.5}$$

The term E, which represents the sum of kinetic energy and potential energy, can be described mathematically as:

$$E = h - \frac{p}{\rho} + \frac{v^2}{2} \tag{2.6}$$

where, h is the sensible enthalpy, k_{eff} denotes the effective conductivity which is $(k + k_t)$. The term k_t is the turbulent thermal conductivity, which depends on the

turbulent intensity of the flow.
The energy transfer due to conduction and viscous dissipation are represented by the first two terms on the right hand side of Equation (2.5) respectively.

2.3 Shear-Stress Transport (SST) k- ω Turbulence model

For the purpose of modeling the turbulence in the flow, the idea was to utilize a 2-equation model to reduce the computational time. Furthermore, the scope of the study did not involve analysis of a number of turbulent characteristics. Hence a 2-equation model would suffice.
The SST k-ω model used was as developed in [15], to provide robust solution with clear distinguishment between the near wall boundary layers and the free stream velocities.

2.3.1 Transport equations for the SST k-ω model

This section pertains to the equations used for modeling of the turbulence kinetic energy, k, and the specific dissipation rate, ω. The following equations are utilized for this purpose[15]:

$$\frac{\partial}{\partial x_i}(\rho k u_i) = \frac{\partial}{\partial x_j}\left(\Gamma_k \frac{\partial k}{\partial x_j}\right) + G_k^* - Y_k + S_k \tag{2.7}$$

$$\frac{\partial}{\partial x_i}(\rho \omega u_i) = \frac{\partial}{\partial x_j}\left(\Gamma_\omega \frac{\partial \omega}{\partial x_j}\right) + G_\omega - Y_\omega + S_\omega \tag{2.8}$$

The term G_k^* depicts the turbulence kinetic energy generation from mean velocity gradients. G_ω represents the generation of ω. The terms Γ_k and Γ_ω depict the effective diffusivity of k and ω respectively. Terms Y_k and Y_ω depict the dissipation of k and ω due to turbulence. The transport models for the individual terms mentioned above can be found in detail from [15].

2.4 Internal Flow

Whenever a fluid flows through a duct or a channel, the inner walls of the duct/channel confine the flow. This state of flow confined by the inner surface of a structure is termed as internal flow. An internal flow follows similar physical laws and governing equations as an external flow, but the conditions developed due to the nature of the geometry, etc are different as will be observed.

Fluid flow can be classified either laminar or turbulent. Laminar flow is defined as when the fluid flowing over the plate flows in clear streamlines with the streamlines being parallel to one another. In case of turbulent flow, the streamlines intersect one

another and there is formation of additional flow qualities such as turbulent eddies, vortexes etc.
There also exists an additional transitional regime between the two flows where the flow is a combination of both laminar and turbulent regime with varied flow properties. A vital tool in determining the nature of flow in a variety of scenarios is the Reynold's number. The Reynold's number is a dimensionless quantity representing the ratio of inertial forces to the viscous forces in a fluid:

$$Re = \frac{Inertial forces}{Viscous forces} = \frac{\rho u L}{\mu}$$

where, u is the velocity of the fluid, L is the characteristic length of the fluid and μ is the dynamic viscosity of the fluid. For fluid flow in a duct, the characteristic length L is defined as the hydraulic diameter (d_h), which can be calculated as [16]:

$$d_h = \frac{2ab}{a+b} \tag{2.9}$$

Where, a and b denote the length and width of the duct respectively. On account of the experimental investigations conducted by Osborne Reynolds, the Reynold's number at which the transition occurs from laminar to turbulent flows has been found to be $Re \approx 2300$ [17].

2.4.1 Thermal Boundary Layer

When the internal fluid has a different temperature compared to the temperature of the solid, a temperature gradient exists between them. This gives rise to gradual heat transfer between the fluid and the solid and can be observed in different fluid layers where the temperature ranges from T_s (Temperature of the solid surface) to $T(r, 0)$ (Temperature of the free stream), as can be observed in Figure 2.1[1]. This gradual variation of fluid temperature from the solid surface to the free stream temperature can be referred to as a "Thermal boundary layer".

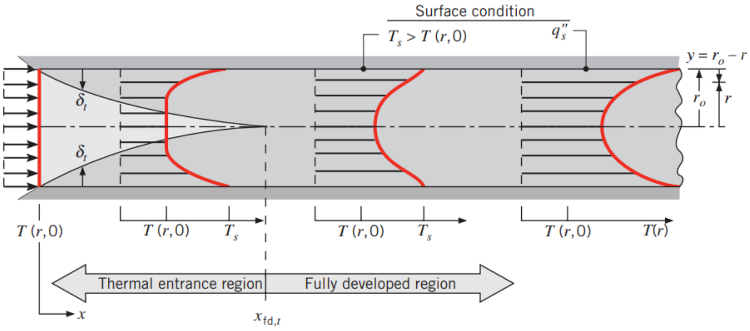

Figure 2.1: Thermal boundary layer development in circular tubes. δ_t represents the thickness of the boundary layer, $q"_s$ the heat flux, and r the radius of the pipe

---

[1] Source: [18]

One can observe the thermal boundary layer to be gradually forming on both sides of the internal geometry until they meet. The distance at which the fully developed thermal profile is formed from the entrance of the geometry is called the thermal entrance length.
The thermal boundary layer is fully formed after the thermal entry length and this region is called fully developed region. It must be noted that all the calculations involved for this study are assumed to be in the fully developed thermal region.

2.5 Convective heat transfer and the Nusselt number

Convection is the mechanism of heat transfer wherein heat transfer occurs between a solid and a fluid in flow. Convective heat transfer is a function of the temperature gradient between the fluid and the solid. This can be mathematically expressed using Newton's law of cooling:

$$q = h\Delta T \tag{2.10}$$

Where, q is local heat flux in W/m^2, h is the coefficient of convective heat transfer, in $W/m^2 - K$ and ΔT is the temperature gradient K.
The Nusselt number(Nu) can be defined as the ratio of convective heat transfer to the conductive heat transfer in the fluid as:

$$Nu = \frac{hL}{k} \tag{2.11}$$

where L is a characteristic length and it is empirically known [18] that for a prescribed geometry,

$$Nu = f(x^*, Re_L, Pr) \tag{2.12}$$

where: and Pr is the Prandtl number, which is the ratio of momentum diffusivity, i.e, kinematic viscosity to the thermal diffusivity of a fluid [19].

As discussed in Equation (2.11) The Nusselt number can be expressed as the function of Reynolds number and the Prandtl number. There exist a number of theoretical correlations for the calculation of Nusselt number. For the purpose of this study, the Dittus-Boelter Equation as introduced by McAdams [20] has been used:

$$Nu = 0.023 Re^{0.8} Pr^{0.4} \tag{2.13}$$

The Dittus Boelter equation is ideally chosen for hydrodynamically and thermally fully developed turbulent flows in circular ducts. However, for the ducts involved in this study, the applicability can be tested.

2.6 Laminar Flow Element

This section pertains to the theory behind the Laminar Flow Element (LFE) used to develop a flow within the wind tunnel chamber in the lab tests.

The flow through the LFE can be explained by the Hagen Poisuille equation [21]:

$$\Delta P = \frac{8\pi\mu LQ}{A^2} \tag{2.14}$$

where, ΔP is the pressure difference across the ends of the LFE, μ is the dynamic viscosity of the fluid (air in this case), L is the length of the LFE, Q is the volumetric flow rate through the LFE, A is the cross sectional area of the LFE.
One can infer from equation 2.14 that if the cross sectional diameter of the LFE is considerably low compared to the overall length, the pressure drop ΔP produced by the LFE is linearly related to the Volumetric flow rate, Q. It must also be noted that the LFE is constructed with a matrix of smaller tubes and hence the diameter of the individual tubes is very little compared to its length. A typical LFE matrix used in most modern day devices can be observed from Figure 2.2:

Figure 2.2: A typical LFE matrix.

Hence, with the low diameter to overall length of individual LFE elements combined with the formation of a matrix, it is possible to generate a laminar flow over a given region while simultaneously controlling the air flow rate in the control region.

3

Design Model

The design model has been developed to minimize the complexity of actual RDs as to only contain the elements that are relevant to the study. Hence, a geometrical design devoid of all chamfers, curved edges and screw holes, was first produced and then manufactured.

The simplification of the design was also done by keeping in mind the necessity of a "clean" Computer Aided Design (CAD) geometry in order to reduce the time required for meshing for the CFD analysis and solving the equations.

After the necessary simplifications, the design model is divided into:

1. **Front cover:** This is the "Front" of the model, as seen in Figure 3.1. This would practically be facing a person on the ground when they observe a RD docked on a pole.
2. **Back cover:** This is the "Back" portion of the model, as seen in Figure 3.1. Positioned in the rear of the docking, it is usually provided with clamps for mounting on poles.

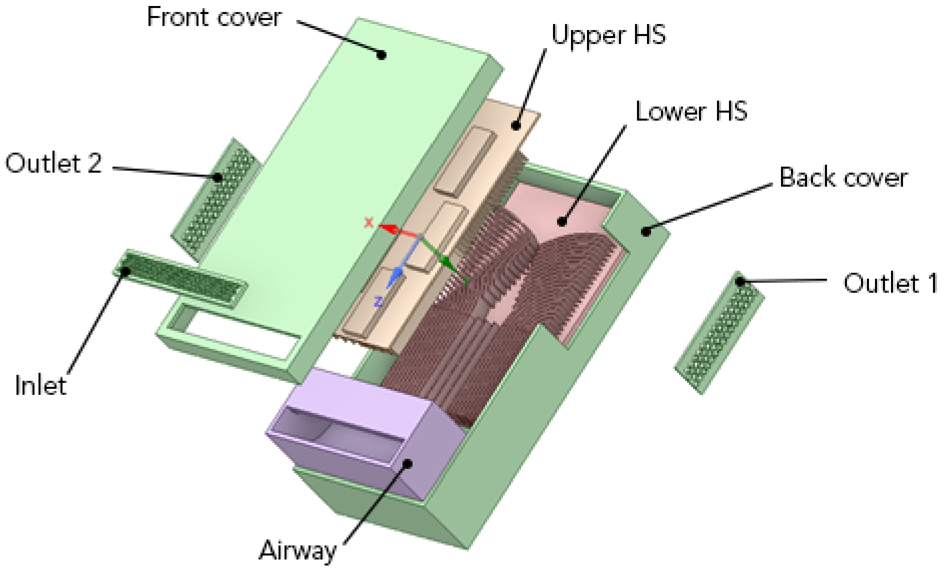

Figure 3.1: Exploded view of the CFD model showing the various listed parts.

3. **Inlet holes:** The inlet holes were designed as a pattern of holes machined on a flat plate which could easily be screwed on to the front cover section. For the purpose of this study, 2 inlet hole patterns were designed, namely:
   (a) Hexagonal holes pattern:
   This hole pattern for the inlet were produced with the dimensions shown in Figure 3.2:

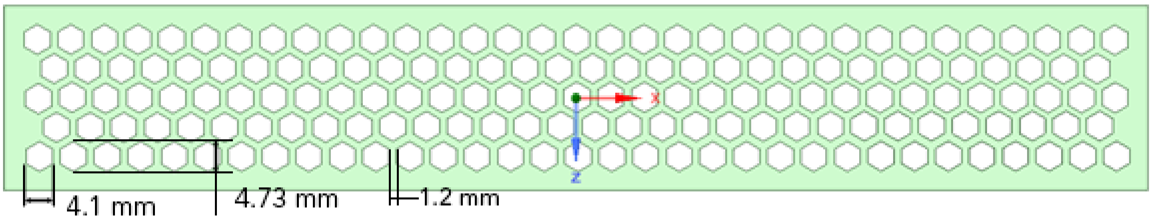

Figure 3.2: Dimensions and pattern for the hexagonal shaped inlet holes.

   (b) Louvers pattern:
   Inspired by the design of medieval European windows [22], this inlet hole pattern has been designed as illustrated in Figure 3.3:

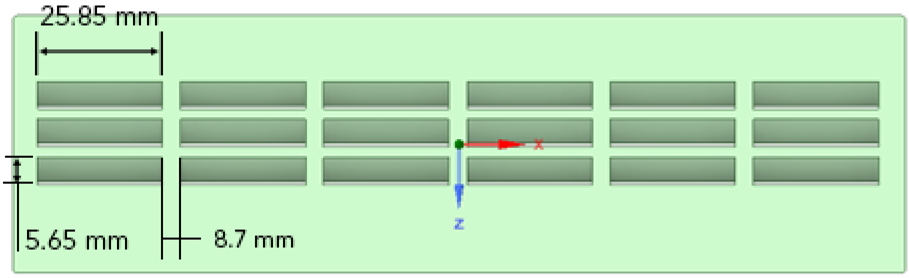

Figure 3.3: Dimensions and pattern for the Louvers shaped inlet holes.

4. **Air channel:** The air entering the radio unit is guided to the internal regions by means of a duct with a 90 degree internal bend to ensure that the flow enters parallel to the heat sinks in the internal regions of the box.
5. **HS:** The HS designed to conduct the heat away from the base of the RD, are as shown in the Figure 3.4 and Figure 3.5.
   It must be noted that 7 raised "platforms" have also been designed on top of the HS plates to facilitate fixture of heaters which simulate the heat generated in an actual radio unit. The positioning and the dimensions of these raised platforms is shown in Figure 3.6.

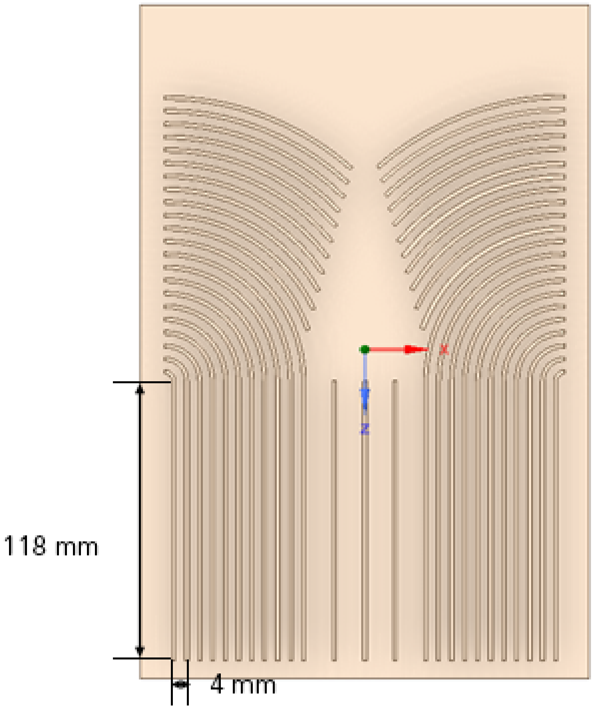

Figure 3.4: Layout and dimensions of the ducts in the Upper HS.

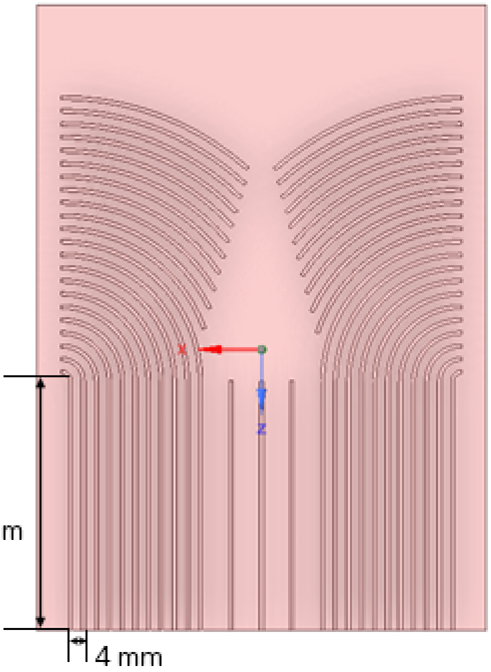

Figure 3.5: Layout and dimensions of the ducts in the lower HS.

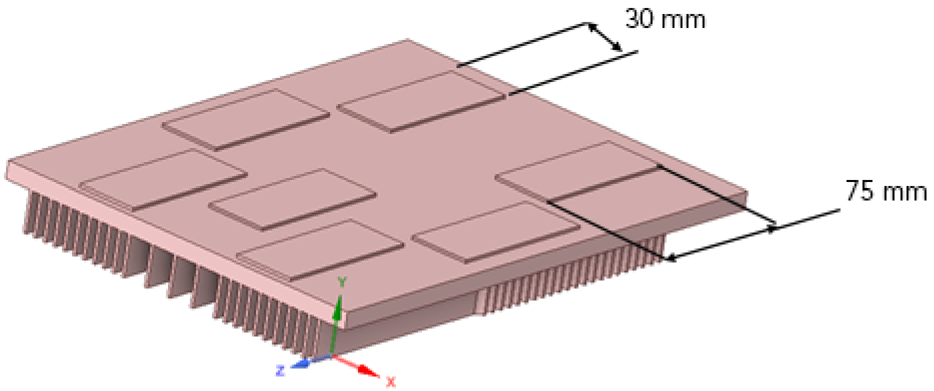

Figure 3.6: Positioning and dimensions of the platforms for placement of Heating elements on the HS.

6. **Outlet holes:** The air outlet for the RD is through 2 regions positioned on the side. Screw-on outlet holes were designed and machined for easy swapping of the hole patterns during lab testing. The outlet hole patterns consisted of 4 designs of which only 2 were considered for lab testing.
   (a) Hexagonal hole pattern: This outlet pattern was similar to the hexagonal inlet pattern. The dimensions for this pattern is shown in Figure 3.7.

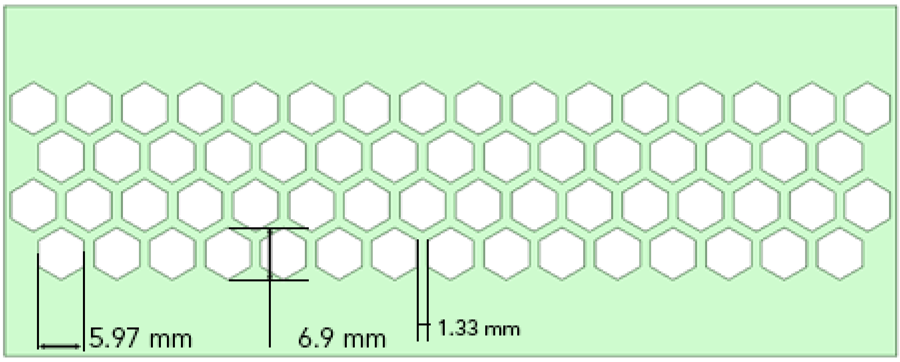

Figure 3.7: Dimensions for the Hexagonal shaped outlet hole pattern.

   (b) Louver pattern: This outlet hole pattern was also similar to the Louver inlet pattern and was designed as illustrated in Figure 3.8.

It must be noted that only the Hexagonal and the Louver patterns were manufactured for lab testing whereas the other hole patterns were only simulated for investigating the desired parameters.

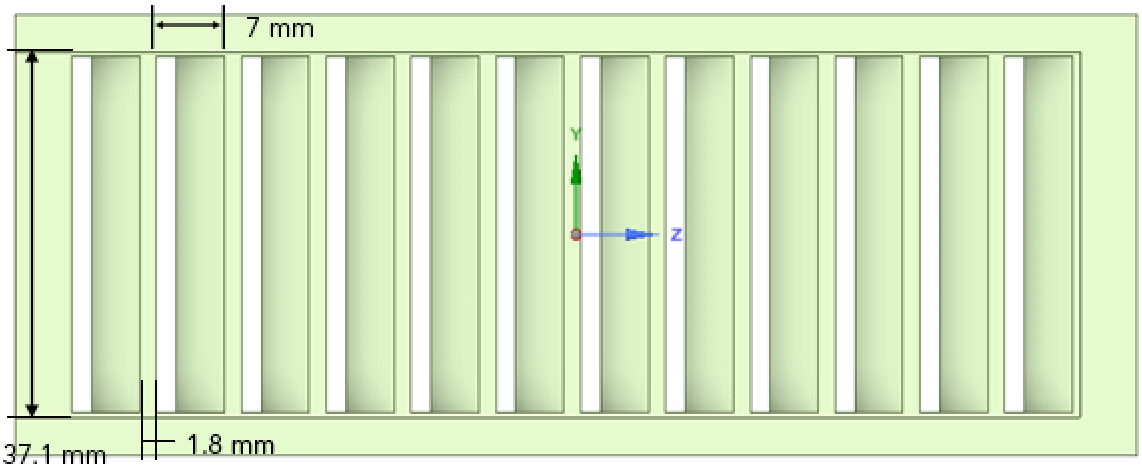

Figure 3.8: Dimensions for the Louvers shaped outlet hole pattern.

(c) Tall stripe pattern:
As the name suggests, this outlet hole pattern consists of thin tall stripes, depicting a slender outlet geometry. The dimensions for this hole pattern are shown in Figure 3.9

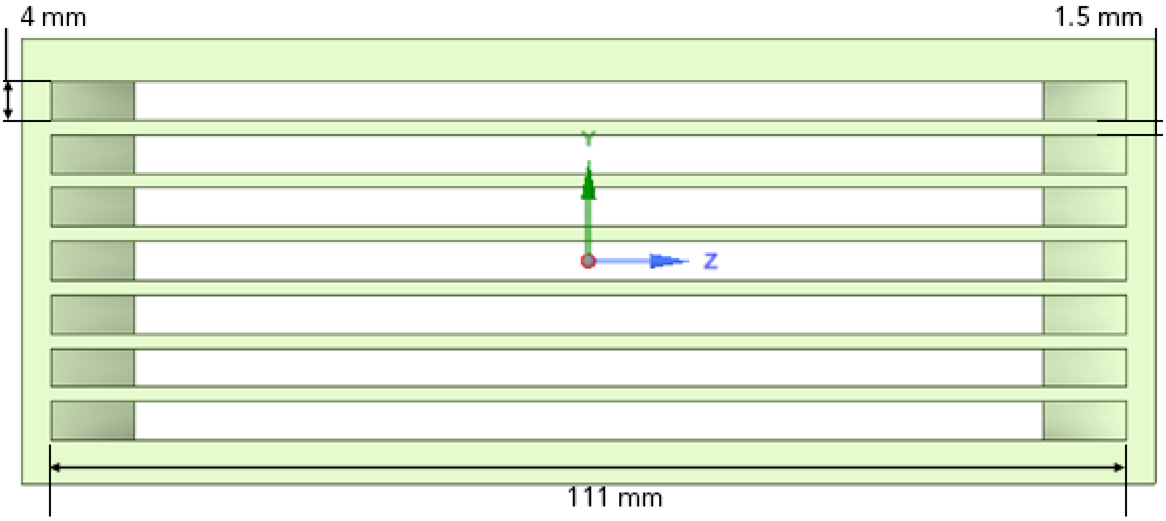

Figure 3.9: Dimensions for the Tall Stripes outlet hole pattern.

(d) Uni gill pattern:
This outlet pattern was not designed as a standalone snap on piece like the others, rather it involves a small slit created between the front and the back covers, facilitating the air flow as shown in Figure 3.10 [b]. The resulting air flow path due to the hole geometry is shown in Figure 3.10 [a]

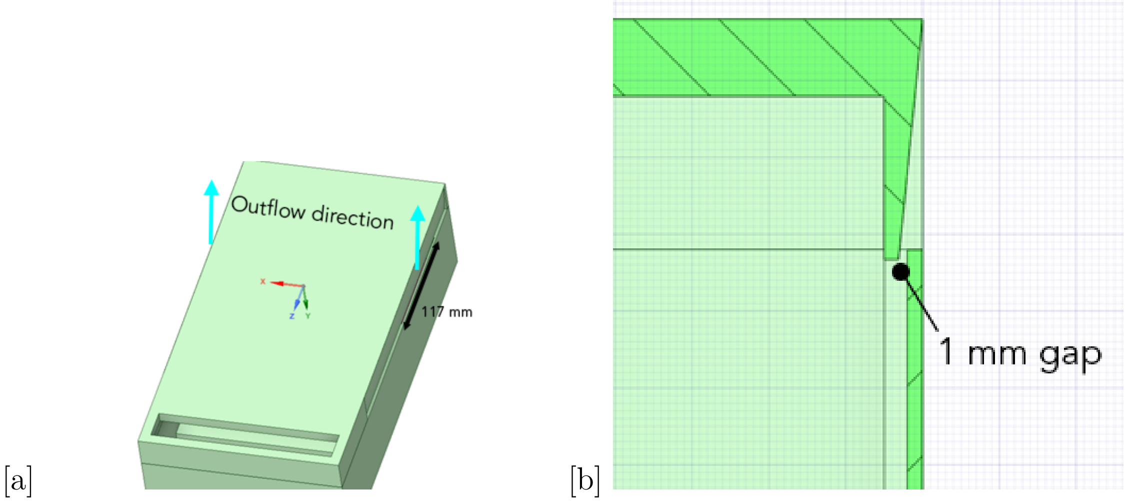

Figure 3.10: [a] Isometric view of the Unigill outlet hole depicting the outflow path. [b] Sectional view of the Front and back covers illustrating the 1 mm gap to form the outlet.

The CFD model is illustrated in Figure 3.1 with all the previously named parts labeled. It must also be noted that the designs manufactured for full scale testing have been substantially tweaked to save manufacturing time and materials required and can be seen in Figure 3.11.

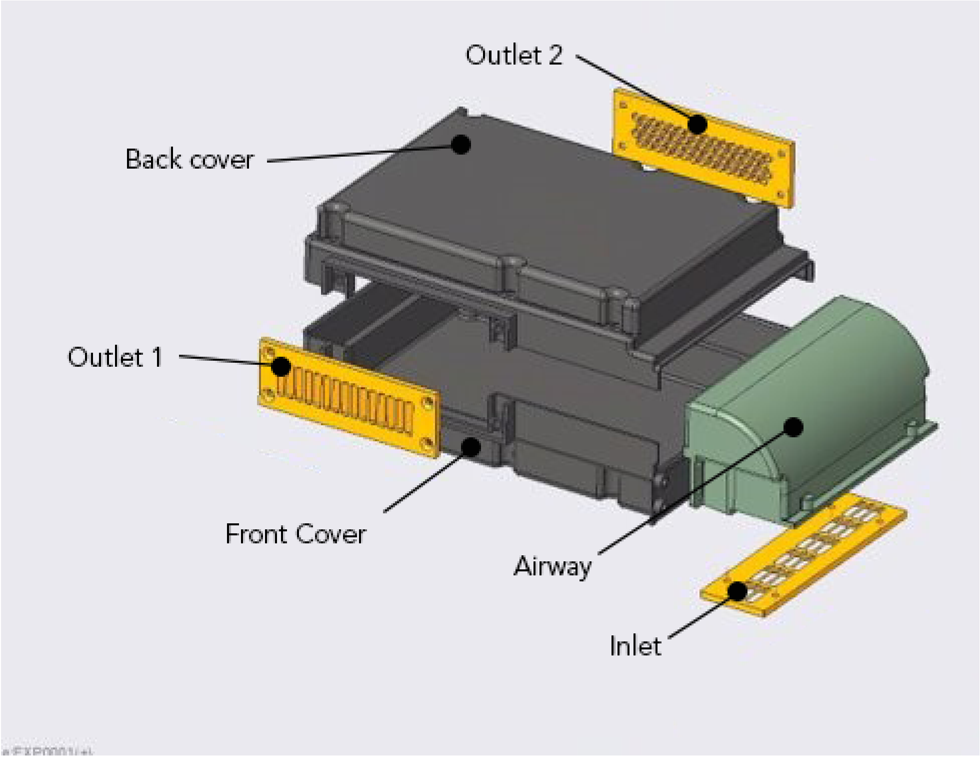

Figure 3.11: Exploded view of the test model showing the design of the manufactured parts.

The materials used for manufacture of were mainly Wrought Aluminium Alloy

(AW6082) and Polylactic Acid (PLA) which is the type of plastic used for 3D printing. The materials for the different parts are listed in Table 3.1.

Table 3.1: List of the parts and the materials used for the respective parts.

Material	
PLA: Front Cover, Back Cover, Air Channel	**AW6082:** Inlet Holes, Outlet Holes, Heat Sinks

An important aspect to be noted is the difference in the inlet and outlet areas among the different hole patterns as this difference can lead to varied inlet and outlet velocities and a varied pressure drop as a consequence. The different areas along with the wetted perimeters, for the reader's reference are listed in Table 3.2. The wetted perimeter refers to the sum of the wetted perimeter of all the holes at the inlet/outlet.

Due to the very low ratio of Outlet-to-Inlet area (0.1:1) for the Unigill model, an additional design was modeled where the Outlet-to-inlet ratio was close to 1. This design will be referred to as Unigill-v2 in this report.

Table 3.2: Inlet and Oulet areas for the different hole patterns.

Pattern	**Inlet area (mm^2)**	**Wetted inlet perimeter (mm)**	**Outlet area (mm^2)**	**Wetted outlet perimeter (mm)**
Hexagonal	2372.94	9520.11	3827.37	7360.64
Louvers	2632.13	1228.32	4389.33	4913.09
Tall stripes	-	-	6216	6515.18
Unigill	-	-	234	952
Unigill-v2	-	-	2106	1016

4

Methodology

4.1 Experimental methodology

This section pertains to the experimental setup and the various parts that are relevant to this project work. The testing of the assembled model was conducted at the lab facilities of Ericsson AB at Kista and a wind tunnel was employed for the purpose of the test. The main goal of the lab testing was to mimic the cooling inside the RD and measure the pressure drop induced by the flow. Consequently, the resulting HS temperatures were also measured.

The measurement of pressure drop is relevant as it signifies the pressure drop that must be overcome by the fan that will be placed in an actual device. This would mean reduced energy requirements for active cooling of the device.

Along with the pressure drop, a lower HS temperature is appreciated as it is also linked with the fan energy requirements for the RD. Correspondingly, the logic with the lab tests was to distinguish between the hole patterns for lower pressure drop and HS temperature values.

- **Definitions**
  Following are the some of the recurring relevant terms used in this section along with their respective definitions:
  - Test unit: This refers to the manufactured replica of the RD observed in this study.
  - Wind Tunnel: This is the air chamber responsible to producing the flow through the test unit. Detailed specifications of the wind tunnel are to be followed in section 4.1.1.
  - Heating elements: These are the elements used to mimic the heat produced in an actual RD. Two types of resistors, 100 Ω (5 No.s) and 150 Ω (2 No.s) were used on each HS as the heating elements in the lab tests (14 heating elements in total).
  - Thermocouples : Type - K thermocouples were used for the measurement of the HS temperature and the temperature readings were recorded using a temperature logger (Pico TC-08$^{\text{TM}}$). Each HS had 3 thermocouples positioned, a total of 6 thermocouples on the HSs. Additionally, 2 thermocouples were positioned at the inlet. They were arranged with the measuring ends suspended in air, to obtain a fairly accurate measurement of the inlet air temperature.

4.1.1 Wind tunnel specifications

The wind tunnel utilized for the lab testing was equipped with a 4 inch Meriam™ LFE. A Ventur™ MPA 50T medium pressure centrifugal fan with the specifications in Table 4.1 was used to generate the flow within the LFE.

Table 4.1: Operating point for the medium pressure centrifugal fan.

Operating point		
Volume flow	441	m^3/h
Air velocity	24.37	m/s
Rotation speed	2789	l/min
Static pressure	1537	Pa
Total pressure	1895	Pa
Dynamic pressure	358	Pa
Power consumption	545	W
Current Intensity	1.24	A
Refulation	50	-
Specific Fan Power (SFP)	4449	$W/(m^3/s)$
Static efficiency	34.5	%
Total efficiency	42.6	%

Theory regarding the functioning of an LFE can be found in section 2.6. Using a step regulator control, the flow required for the various flow rates for the test cases were calibrated. The entire setup of the wind tunnel can be observed from Figure 4.1.

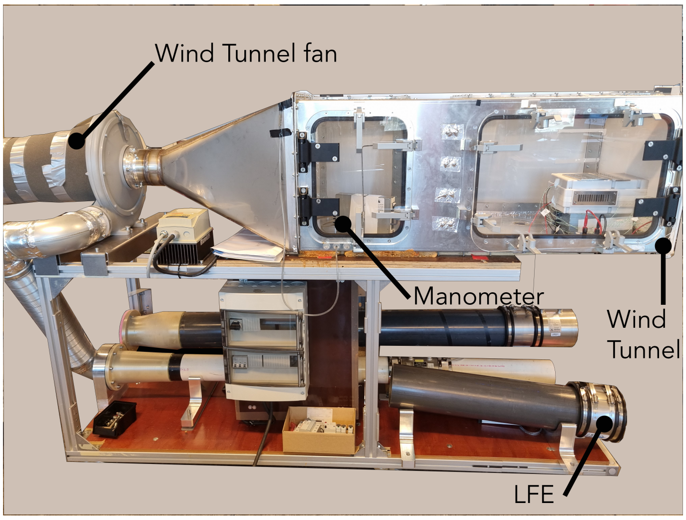

Figure 4.1: Setup of the wind tunnel used in the lab tests

4.1.2 Experimental setup

The experimental setup consists of the following major parts:

1. **Wiring and positioning of the heating elements:**
   The heating elements were screwed on to the HS and a minimal amount of thermal paste was used to evenly disperse the heat on the HS surface. A total of 386 W was applied across both the HS and a parallel wiring scheme was used in case of the resistors. The positioning of the heaters and the thermocouples on the HS can be observed from Figure 4.2.

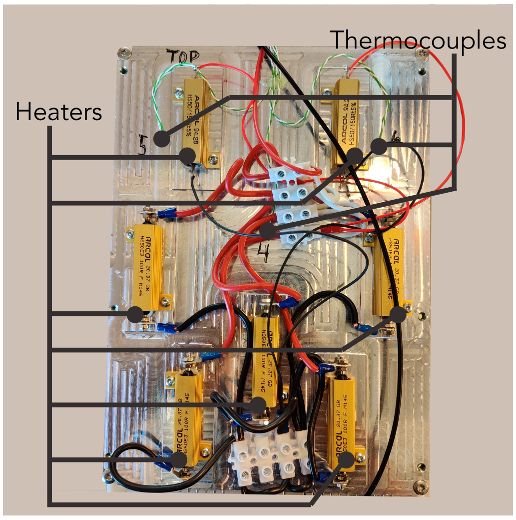

Figure 4.2: Positioning of the thermocouples and heating elements on the HS.

2. **Positioning of Thermocouples on the HS:**
   The thermocouples were placed on the side of HS that had no air flow over it. This positioning ensured that the thermocouples only measured the temperature of the HS and not the air flowing over it
   The thermocouple readings from the inlet during the duration of the test is used to obtain an average inlet temperature for the CFD simulations.

   The data obtained around the HS positions was averaged to obtain an average core temperature.
   The thermocouple data was read using a data logger. The same was used for asserting if a steady state was reached by the HS temperature or not. "Pico Temperature logger TC-08$^{\mathrm{TM}}$" has been used for this purpose.

3. **Positioning of the test unit in the wind tunnel:**
   The test unit was positioned in the wind tunnel to allow for only the inlet to be present outside the wind tunnel while the rest of the units body was maintained inside. To ensure that the air flow was only through the inlet holes, the test unit was thoroughly packed and sealed. The positioning of the test unit can also be observed from Figure 4.3.

Figure 4.3: Positioning of the test unit at the entry of the wind tunnel.

4. **Measurement of pressure drop across the test unit:**
   The pressure drop across the test unit was measured relative to the atmospheric pressure by means of a pitot tube positioned at the end of the wind tunnel as shown in Figure 4.1. For the purpose of the lab tests, the pitot tube SwemaMan 80 ™ was used. It was also positioned so that the reduction in the velocity following the exit of the test unit and the resulting dynamic pressure could be captured to the maximum extent.

4.1.3 Experimental Factors

The two major varying factors across all the lab tests were:

1. **Flow rate through the wind tunnel:**
   The flow rate through the wind tunnel was motivated for the operating points for the fan used in an actual RD. The idea was to mimic the flow through the test unit as an actual RD.
   The aforementioned fan curve can be observed from Figure 4.4. For the purpose of the lab tests and the CFD simulations, Operation Point 1 (OP1) and OP2 were considered, along with an intermediate value between OP2 and OP3.

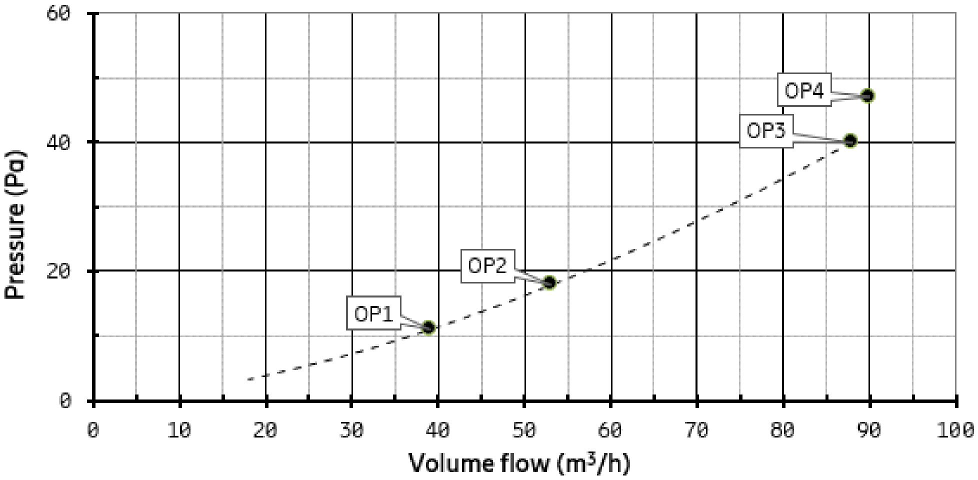

Figure 4.4: Fan curve of the cooling fan used in the actual RD.

2. **Inlet and outlet hole patterns:**
   As mentioned in section 3, only the hexagonal holes pattern and the louvers pattern were considered for the lab tests.

The combination of these experimental factors resulted in the various cases that were studied, and will be explained in detail in section 4.1.4

4.1.4 Test cases

The following are the test cases considered for this study. It must be noted that both the hexagonal and the louvers hole patterns were subjected to similar flow rates closest to 0.5 m^3/h between successive Hexagonal and Louver cases[1].

Table 4.2: Various cases considered for the lab test along with their experimental factors.

Case	Inlet Pattern	Outlet Pattern	Flow rate (m^3/h)
1	Hexagonal	Hexagonal	35.1
2	Louver	Louver	34.84
3	Hexagonal	Hexagonal	56.14
4	Louver	Louver	56.4
5	Hexagonal	Hexagonal	71.77
6	Louver	Louver	72.16
7	Hexagonal	Louver	36.15

Using the maximum area from Table 3.2 and the maximum flow rate from Table 4.2, air velocity can be calculated to get a measure of the nature of the flow.

---

[1] The motivation for case No. 7 will be explained in section **??**

$$U_{\text{air}} = \frac{72}{4389.33} * \frac{10^6}{3600}$$

The resulting air velocity ($U_{\text{air}} = 4.56$ m/s) is too low ($\backsim$ 0.01 Mach), further supplementing the fact that the problem under consideration is an incompressible flow situation.

4.2 CFD simulations

The simulations were carried out on ANSYS Fluent$^{\text{TM}}$2021 R2. The same was used for mesh generation and post processing analysis as will be explained in further sections.

4.2.1 Simulation domain

The domain for the CFD simulations was created keeping in mind the dimensions of the wind tunnel and the positioning of the RD inside the wind tunnel to increase the accuracy and legitimacy of the simulation results. The simulation domain along with the positioning of the RD can be seen in figure 4.5.

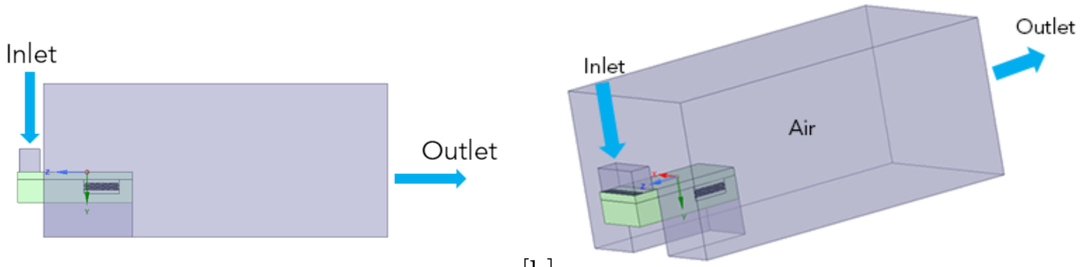

[a] [b]

Figure 4.5: Simulation domain used for the CFD simulations.

4.2.2 Mesh quality and metrics

As mentioned previously, the meshing of the simulation domain was carried out on ANSYS Fluent$^{\text{TM}}$, with polyhedral cells generated in both the solid and the fluid domain. Usage of polyhedral cells produced good mesh metrics and enabled better prism layer generation near the walls. Due to this, near wall effects on the fluid were also captured in detail at fluid-solid interfaces. The mesh generation and the development of prism layers along the walls in the regions of interest can be observed from Figure 4.6.

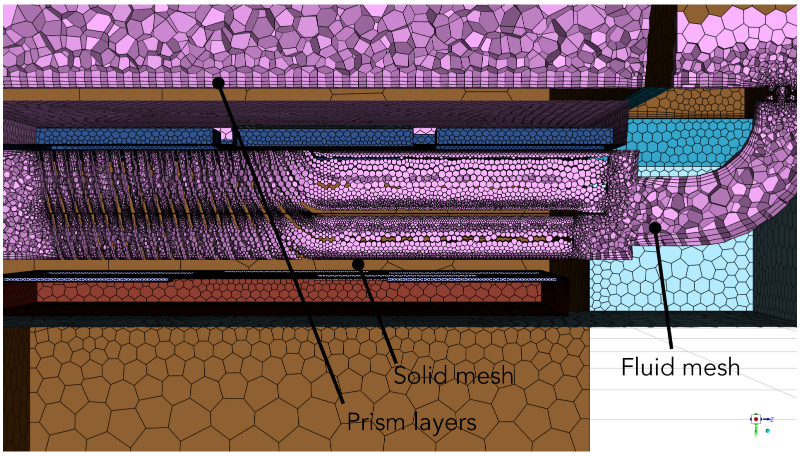

Figure 4.6: Section plane showing the mesh generation on the solid and fluid volumes inside the RD.

The mesh metrics were observed to be good, with orthogonal quality of 0.1-1 within the RD and a cell count of 5.2 Million was observed in the global simulation domain.

4.2.3 Problem setup along with boundary conditions on ANSYS Fluent

The major boundary conditions set up on ANSYS Fluent were:

- **Inlet**:
  Mass flow inlet - with the mass flow corresponding to the cases from Table 4.3. A thermal condition was set up for the inlet air temperature at 22 °C (295 K). Additionally, no slip condition was set up at all walls, ensuring 0 fluid velocity at those positions.
- **Heating elements wall flux**:
  A constant wall heat flux at the position of the heating elements was specified as calculated in Section 4.2.4.
- **Outlet**:
  At the outlet, a pressure outlet boundary condition has been used (∇P=0). This means that by specifying a gauge pressure at the outlet, the outflow conditions are calculated with refernce to the inlet conditions.

4.2.4 Calculation of heat flux through the heat sinks

The dimensions of the platform upon which the heating elements were placed can be seen from the Figure 3.6. From these dimensions, the heat flux can be calculated as:

Combined area for application of heat flux $= 30 \times 75 \times 14 = 31500\ \mathrm{mm}^2 = 0.0315\ \mathrm{m}^2$;

Heat applied at the positions $= 376$ W;

Heat flux $= \frac{376}{0.0315} = \mathbf{11936.51\ W/m^2}$

To maintain adherence to the experimental study, the cases formulated to be run for the CFD simulations used the same mass flow rate[2] as a factor and the respective scenarios for cases can be observed from Table 4.3. Along with these scenarios, the cases that will be run for the different hole pattern combinations can be observed in Table 4.4.

Table 4.3: Flow rates for the different simulation scenarios that will be run.

Scenario	**Flow rate (m3/h)**	**Flow rate (kg/s)**
1	35	0.0119
2	56	0.019
3	72	0.024

Table 4.4: Different simulation scenarios for the corresponding hole patterns on ANSYS Fluent.

Inlet	**Outlet**	**Cases**
Hexagonal	Hexagonal	1,2,3
	Louvers	1,2,3
	Tall stripes	1,2,3
	Uni-Gill	1
	Uni-Gill 2.0	1
Louvers	Louvers	1

---

[2] The mass flow rate in kg/s was calculated by using properties of air at 22 °C.

5

Results and Analysis

For better understanding of the contents of this chapter, it has been divided into 2 main sections namely, Experimental results and CFD results. The analysis of the results has been carried out individually in both the sections.

5.1 Experimental results

Having conducted the various tests mentioned in Section 4.1.4 and taken the readings for the temperatures and the pressure drops, the results have been tabulated in Table 5.1. For the different inlet and outlet hole patterns[1], contrasting results can be observed.

Table 5.1: Results from the tests for the various cases

Case	**Inlet pattern**	**Outlet pattern**	**Temperature lower HS [°C]**	**Temperature upper HS [°C]**	**ΔP [Pa]**
1	Hexagonal	Hexagonal	62.08	65.45	17.5
2	Louver	Louver	68	65.22	38.5
3	Hexagonal	Hexagonal	51.2	53.82	40.9
4	Louver	Louver	55.6	52.65	94.4
5	Hexagonal	Hexagonal	46.41	48.66	48.66
6	Louver	Louver	50.23	47.36	150.5
7	Hexagonal	Louver	63.72	66.5	24.3

It was noted during the lab tests that the Louvers inlet pattern produced acoustical noise, upon covering the different sections of the hole pattern, the noise resulted in different tones. Since acoustical noise generation is outside scope of this study, one additional case[2] was tested with the lowest air flow rate used in the tests. This case was run with the hexagonal inlet to investigate the sensitivity of the results to the inlet pattern. It must also be noted that the different cases were run in the lab tests until a steady-state temperature was reached on the HS thermocouple readings, as can be seen in Figure 5.1[3].

Since the tests were run with the lowest flow rates in the earlier trials, which would mean the highest temperatures for the HS, it was observed that 1 hour was needed

---

[1] The average inlet air temperature reading during the lab tests was 22 °C

[2] case 7

[3] To reduce the time required for the HS to get heated up, the air flow through the wind tunnel was stopped and it can be observed from 5.1 [b]

for the HS temperatures to stabilize, following which 15 to 20 minutes would be sufficient for the HS to cool down and stabilize during the next test case.

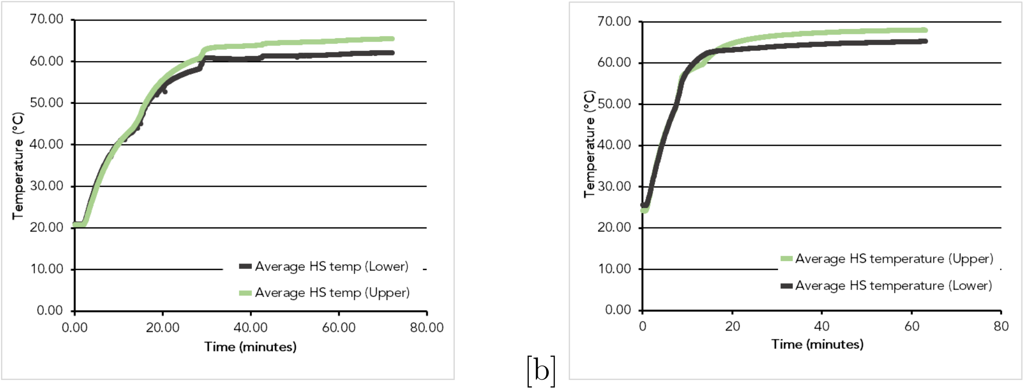

[a] [b]

Figure 5.1: Progression of HS temperatures until steady-state is reached in [a] Hexagonal outlet pattern [b] Louver outlet pattern.

One can notice the gradual increase in the pressure drop at the different flow rates from Figure 5.2 [a]. The increased pressure drop with the louvers pattern can also be correlated to the increased outlet and inlet area with the louvers pattern.
The obtained temperatures on the upper and lower HS during the lab tests have been shown in Figure 5.2 [b].

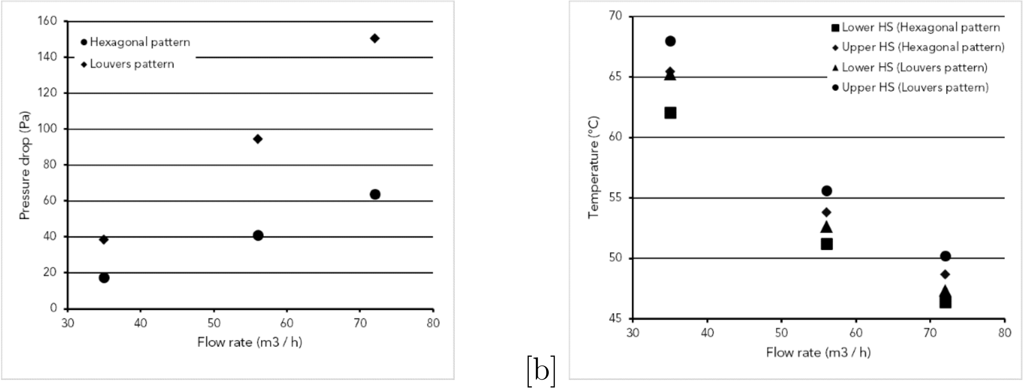

[a] [b]

Figure 5.2: Results from the tests: [a] Pressure drop variation and [b] HS temperature reduction, for the various flow rates.

5.1.1 Experimental result analysis

The higher values for the Upper HS and lower values for the lower HS with the Louver inlet, when compared to the Hexagonal inlet indicate the air flow being directed towards a particular direction and hence resulting in increased cooling.
From Table 5.1, it is evident from the difference in case 2 and case 7 the Louver style inlet influences the HS temperature by redirecting the air flow.

A good measure for comparison exists between case 1 and case 7 as both have a common inlet design and only a different outlet hole pattern. The difference in

obtained test results are shown in Table 5.2. Intuitively, one can observe that a greater outlet-to-inlet area ratio would result in lower air velocities [4] and hence an increased pressure drop.
The nature of the obtained temperatures will be dwelled upon in further sections.

Table 5.2: Difference in test readings between case 1 and case 7.

Case	**Outlet Area / Inlet Area**	**Upper HS Temperature [°C]**	**Lower HS Temperature [°C]**	**ΔP [Pa]**
1	1.61	65.45	62.75	17.5
7	1.85	66.5	63.72	24.3

5.2 CFD results

For a better understanding of the nature of the results observed, before we move to the results, a few validation checks have been carried out on the CFD results. As these are crucial in holding the integrity of the solution, they will be made clear in the sections to be followed.

5.2.1 Convergence and residuals

Before proceeding to analyze the CFD results, it is important that the convergence of the solution is attained, i.e, the variations in the numerical calculations reach a minimum value ($\backsim$ 2%) [23].
Convergence is important in analyzing the nature of the solutions as it is not possible to know the exact solution to the PDEs solved in the governing equations. Hence the residuals are monitored to the point of least fluctuation in the results across the different iterations.
After 250 iterations, the residuals do not further reduce and are reasonably stable, as can be observed from Figure 5.3. One can move forward to check if the convergence criteria is met by checking the convergence monitor.

---

[4] The lower air velocities are related to conservation of mass as the air flow rate is same in both the cases.

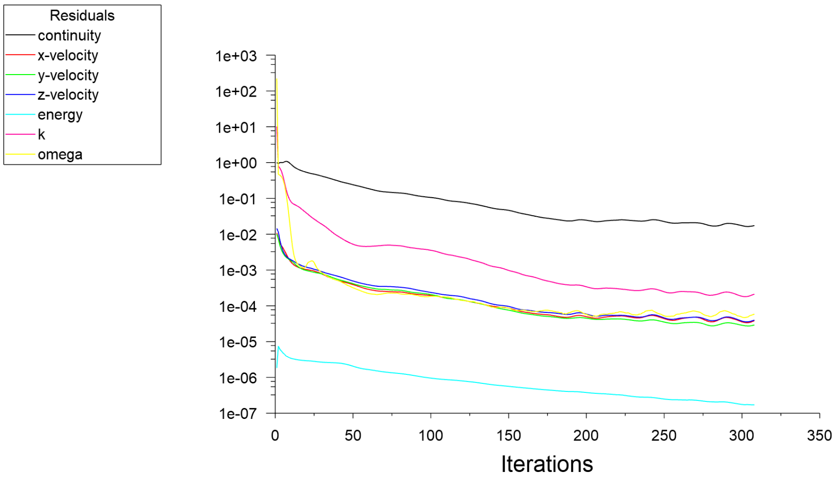

Figure 5.3: Variation of the residuals as the CFD calculative iterations progress.

The convergence of the CFD solution has been assured the conservativeness of the solution. This has been done by observing the mass imbalance at the outlet, i.e, if the mass flowing out of the domain is same as the amount of mass flowing in. One can observe the mass conservation in the domain from Figure 5.4.

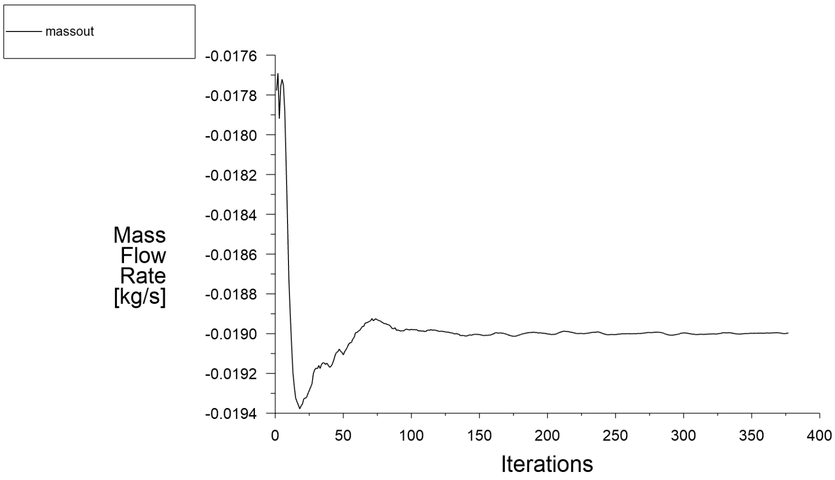

Figure 5.4: Mass flow rate at the outlet of the CFD domain. The flow rate at the inlet was 0.019 kg/s.

Following the observations in Figure 5.3 and Figure 5.4, the solutions can be concluded to have converged and one can proceed to analyzing the results.

5.2.2 Mesh sensitivity test results

In conjunction with the monitoring of the residuals and the mass imbalance for convergence of the solution, a mesh sensitivity test was conducted to further establish the independence of the obtained solutions on the nature of the grid used or any numerical anomaly.

The purpose of the grid independence test is also to minimize the errors obtained due to inadequate size/number of cells in regions of interest [23]. The mesh sizes used for the test and the resulting pressure drop obtained across the RD can be observed from Figure 5.5.

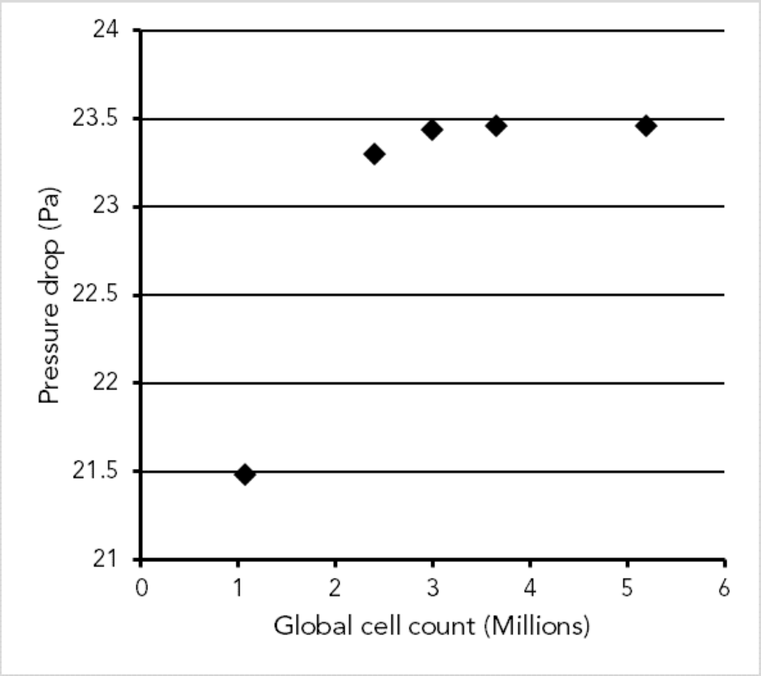

Figure 5.5: Results of the mesh independence tests.

It can be observed that the error in the pressure drop calculations reduces to 0.5% ∽ 1% and mesh independence can be observed to have been achieved at 3 Million cells.

5.2.3 Results for Pressure drop and HS temperatures

For the CFD simulations, a total of 12 cases were studied, and the resulting values for the temperatures and the pressure drop can be observed from Table 5.3.

Table 5.3: Results from the CFD simulations for the different cases.

Hole Pattern		**Case**	**Temperature Upper HS [°C]**	**Temperature Lower HS [°C]**	**ΔP [Pa]**
Inlet	**Outlet**				
Hexagonal		1	70.6	69.7	23.5
		2	56.3	55.7	58.3
		3	50.6	49.6	91.5
Louvers		1	73.7	65.5	51.6
Hexagonal	Louvers	1	72.2	69.5	21.1
		2	57.9	55.5	52.8
		3	51.9	49.5	85.08
Hexagonal	Tall Stripes	1	68.4	68.2	20.4
		2	54.9	54.5	49.4
		3	49.2	48.6	80.5
Hexagonal	Unigill	1	69.2	70.1	36.8
	Unigill 2	1	71.9	71.9	1501.6

One can observe a slight difference between the results for the pressure drop with the values from Table 5.1. One of the reasons for this could be the flaws in the experimental setup like leakage through the air chamber, calibration errors, etc., which could result in inaccurate pressure drops and reduced flow through the RD. The variation of pressure as the flow moves through the RD can be observed[5] in Figure 5.6. The pressure difference was measured between the inlet and the position at which the pitot tube was placed in the wind tunnel.

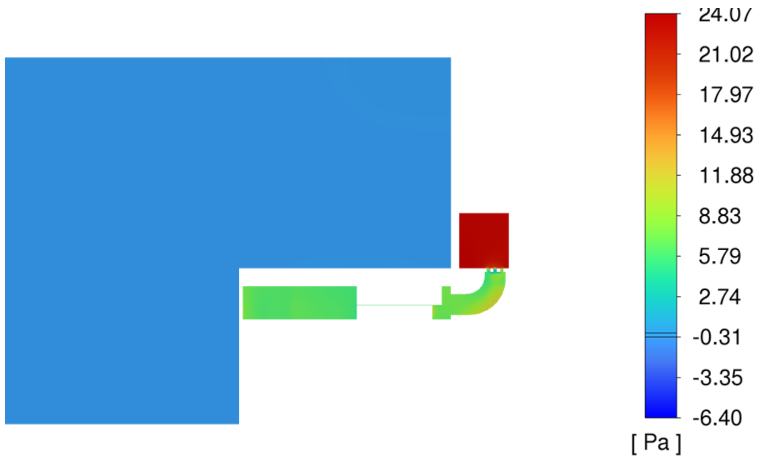

Figure 5.6: Contour of a pressure surface through the RD in the XY plane.

The implications of inaccurate flow through the RD can also be seen in the variation of temperatures of the HS. However, these values have appreciable variations (∽ 11%) and can still be used for comparison with the experimental tests.

The increase in the pressure drop with increasing flow rate for the different test cases can be observed in Figure 5.7. It is interesting to note that the Tall stripes pattern, having the largest outlet-to-inlet area ratio, as seen in Table 3.2 has the

---

[5] The pressure surface corresponds to simulation data of case 1 with the hexagonal outlet pattern

lowest pressure drop for each case.
One can also observe the excessive pressure drop obtained from the Unigill pattern. Possibly a consequence of the poor outlet-to-inlet ratio, this case has not been included in Figure 5.7 to maintain the scale of the plot.

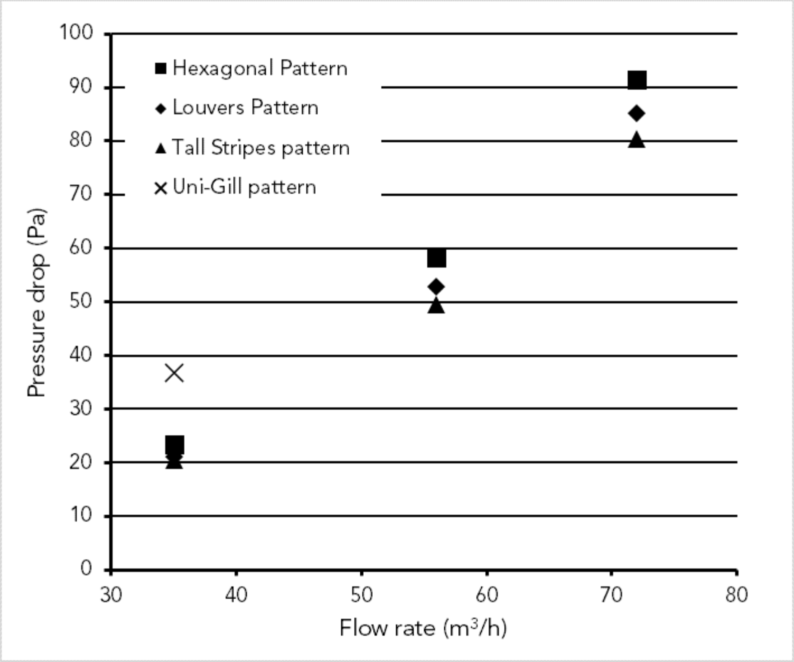

Figure 5.7: Pressure drop obtained across the RD for the different outlet hole patterns.

The nature of the temperature of the HS upon increasing flow rates for the different cases can be observed from Figure 5.8. Similar trend can be observed as the experimental results for both the hexagonal and the louver outlet geometries.
It is interesting to also note that the Tall Stripe outlet performs better on both the Upper and the Lower HS temperatures in all the cases.

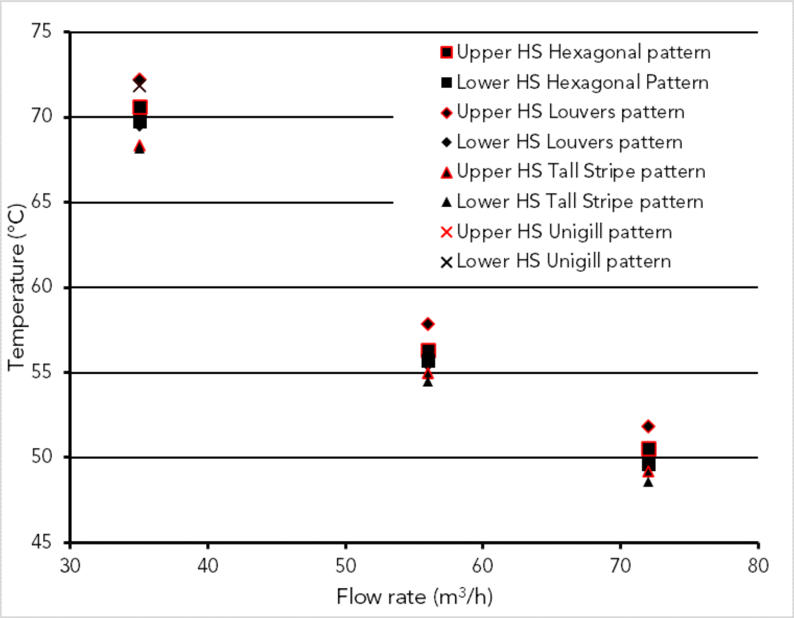

Figure 5.8: Temperatures of the Upper and Lower HS with the different outlet hole patterns.

5.2.4 Calculation of Reynolds numbers

For analysis of the flow through the HS, the Reynolds number for the respective duct of the HS needs to be calculated. The geometries of the upper and lower heat sinks along with the respective dimensions can be observed from the Figure 3.4 and Figure 5.9.
Using Equation 2.9, the hydraulic diameters for the heatsinks can be calculated as:

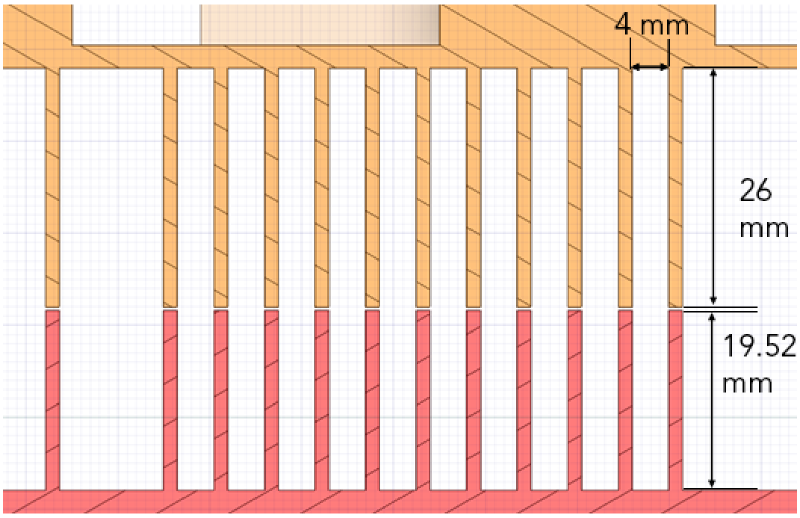

Figure 5.9: Dimensions of the HS duct for calculations of Reynolds number.

Upper HS:
a = 0.004 m; b = 0.026 m; d_h = 0.006933 m

Lower HS:
a = 0.004 m; b = 0.01952 m; d_h = 0.006639 m

Using the respective hydraulic diameters, the Reynolds numbers for the HS were calculated on ANSYS Fluent as a user-defined function and the resulting values are listed in Table 5.4.

Table 5.4: The results for Reynolds numbers (Re_1 and Re_2) in locations of the upper and lower HS in the CFD simulations.

Hole Pattern		**Case**	**Re_1**	**Re_2**
Inlet	**Outlet**			
Hexagonal		1	862	1063
		2	1636	1999
		3	1727	2014
Louvers		1	955	1042
Hexagonal	Louvers	1	875	1075
		2	1525	1700
		3	1896	2063
Hexagonal	Tall Stripes	1	950	1125
		2	1627	1803
		3	2077	2245
Hexagonal	Unigill	1	831	864
	Unigill 2	1	800	980

Combining the results from Table 5.3 and Table 5.4 one can notice that the best performing Outlet pattern, in terms of HS temperatures which is the Tall Stripes pattern, also has the highest values for the Reynolds numbers in all the cases. This is an expected result, since the heat transfer coefficient of the air flowing through the HS ducts increases with increasing Reynolds numbers.

This trend is better illustrated in Figure 5.10 where both the Upper and Lower HS temperatures are plotted as a function of the Reynolds number in the respective ducts. In general one can notice a reduced HS temperature with increased Reynolds numbers in the ducts.

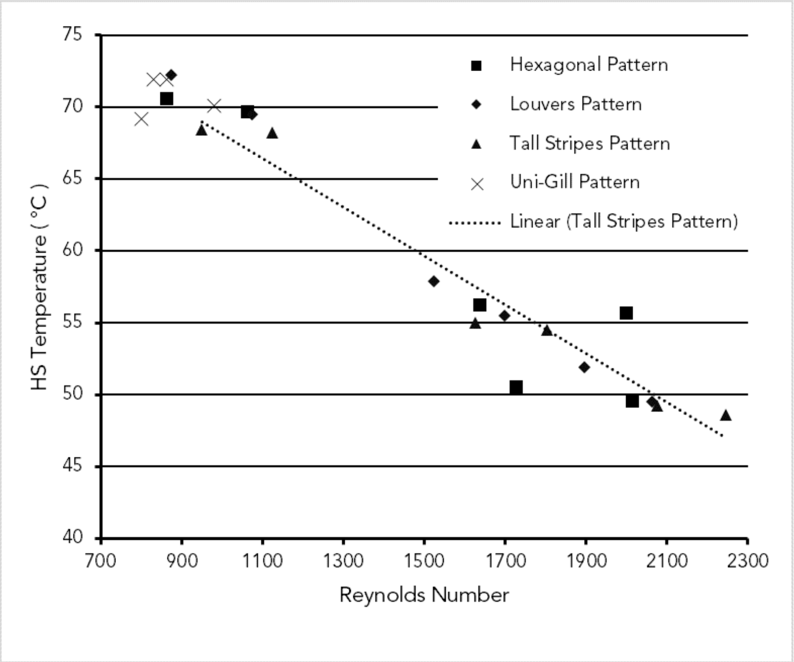

Figure 5.10: Relation of the overall HS temperatures with the internal Reynolds numbers obtained in the RD with the different outlet hole patterns.

5.2.5 Post processing and analysis

Due to the nature of the study being one involving CFD analysis, it is common to include a variety of figures and plots for analysis. To keep the conents of this section short and precise, only the most interesting phenomena observed in post processing will be discussed here.

5.2.5.1 Nusselt number calculations

As mentioned in Section 1.1, the Nusselt number relation for the fully developed flow region was used as a User defined function on ANSYS Fluent. Owing to the uncertain nature of the thermal entry length, a length of about 75% of the duct length was used for these calculations.
Additionally, the Reynolds number in the duct and the respective Nusselt numbers calculated have been shown in Table 5.5.

Table 5.5: Reynolds numbers for the Upper and Lower HS and the respective Nusselt Numbers that were calculated.

Outlet	**Re1**	**Re2**	**Nu1**	**Nu2**
Hexagonal	862	1063	4.65	5.63
Louvers (Louvers inlet)	955	1042	5.32	6.85
Louvers (Hexagonal inlet)	875	1075	4.6	5.6
Tall stripes	950	1125	5.19	5.9
Unigill	831	864	4.66	4.81
Unigill 2	800	980	4.4	5.3

At the position where fully developed flow is assumed, a plane surface showing contours of the calculated Nusselt number has been shown in Figure 5.11.
The calculated Nusselt numbers are also in accordance with the Nusselt numbers for laminar internal flow through ducts with constant heat flux as mentioned in literature [17].

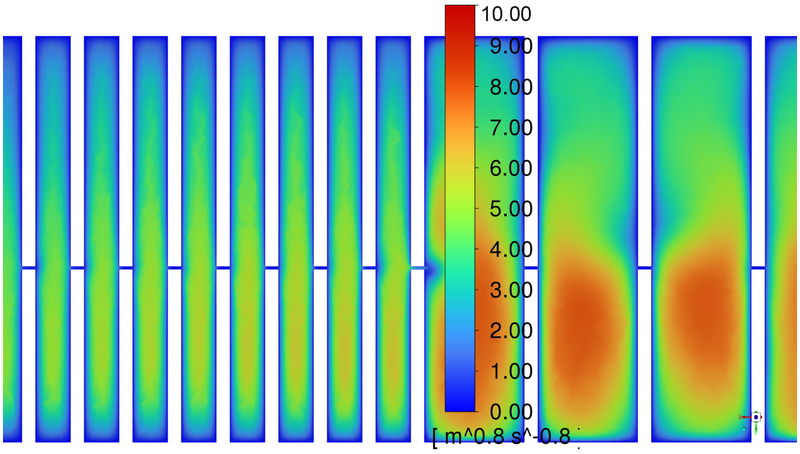

Figure 5.11: Contours of Nusselt number in the HS ducts.

Since the Nusselt number can be used as a measure of the convection heat transfer in a particular region, a curve to show the temperature of the HS with the different Nusselt numbers calculated is shown in Figure 5.12. A general trend of reduced HS temperature with increased Nu can be seen.

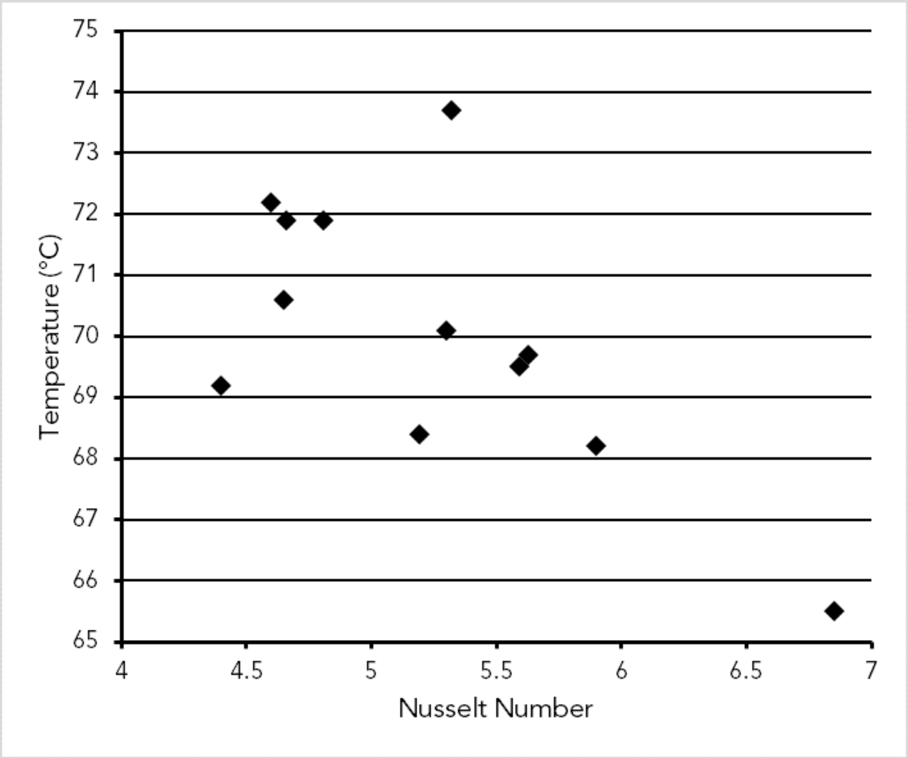

Figure 5.12: The HS temperatures for the points at which Nusselt numbers were calculated.

5.2.5.2 Analysis of the Louvers inlet pattern

It was noted in Section 5.1.1 that the distribution of temperatures on the HS indicated a redirection of the flow due to the inlet geometry. From Figure 5.13 it can be seen that this is indeed true and it could also be hypothesized that the generation of vortices in the entrance and the aiway ducts could be the cause for the generation of acoustical noise by this type of inlet.

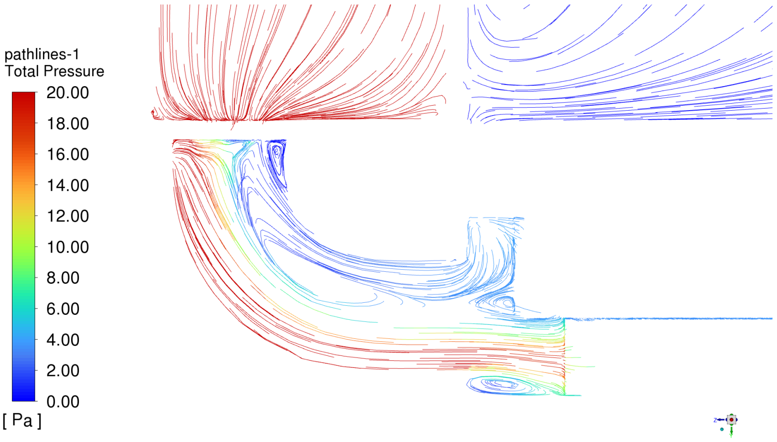

Figure 5.13: Flow redirection and resulting pressure increase due to the Louvers inlet pattern.

5.2.5.3 Pressure buildup inside the RD with the Unigill outlet

The Unigill outlet with the initial design resulted in excessive pressure drops and was remodeled for better performance metrics. The Unigill 2.0 outlet performed better on the pressure drop metrics. However, upon further analysis it was observed that the pressure drop within the RD was very low and all of the pressure drop occurred at the outlet, as the air left the RD.
Upon comparing Figure 5.14 and Figure 5.15, it can be observed that the obstruction to the flow due to shape of the outlet in the Unigill design results in the increased pressure buildup inside the RD and high outlet velocities. This could be a cause for concern when docking the RD along with other devices as the outgoing air stream could affect the ventilation of nearby devices.

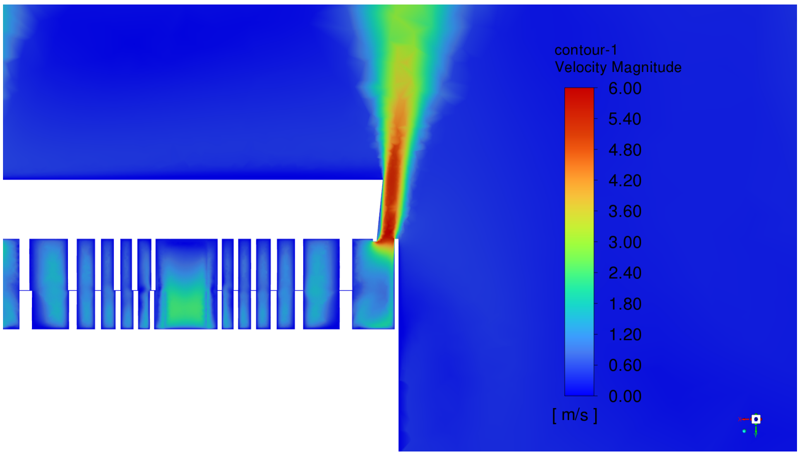

Figure 5.14: Outlet flow velocities with Unigill design.

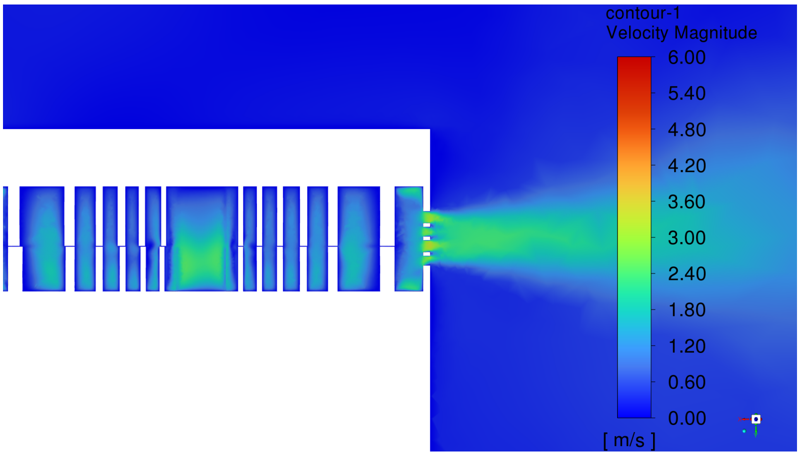

Figure 5.15: Outlet flow velocities with Hexagonal design.

The decision to increase the outlet gap in the Unigill 2.0 model also introduced increased re circulation inside the box which could have contributed to the pressure development inside the box, illustrated in Figure 5.16. A possible way to reduce the side effects of this outlet design would be to introduce a more curved duct at the outlet so that the flow obstruction is reduced and a smoother velocity reduction can be observed at the outlet.

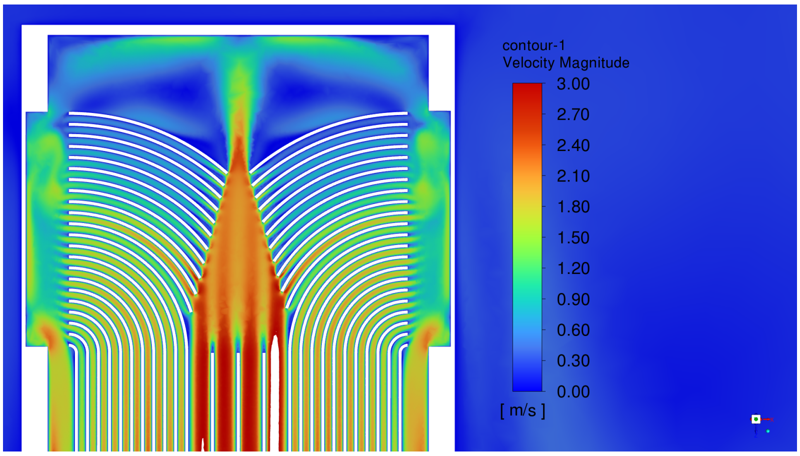

Figure 5.16: Re circulation near the outlet of the Unigill 2.0 design.

6

Conclusion

Experimental tests and CFD analysis were conducted to study the effect of the outlet geometry on the internal flow within the RD. The performance of different outlet geometries was measured based on the pressure drop produced as a result of the internal flow, and the HS temperatures obtained as a result of cooling due to the air flow. In the experimental tests, a model of the RD was placed within a wind tunnel to mock the air flow and cooling of the RD. A number of tests were conducted with two types of outlet hole patterns at different air flow rates through the RD. The experiments were successful at measuring the performance of the outlet hole patterns to some extent and the readings of the HS temperatures also proved to be valid.

The CFD simulations were conducted to replicate the experimental setup and the ambient conditions. Additionally two more outlet patterns were tested in the CFD simulations. The analysis shows that the Tall Stripes pattern performs the best when compared to the other outlet geometries. A combination of the outlet-to-inlet area ratio, higher Reynolds numbers in the HS and lower HS temperatures are a good measure of the hole patterns performance.

The Louvers style outlet geometry performed fairly better but the noise development due to this pattern needs to be kept in mind and further investigation needs to be done.

The Uni gill model proved to be the poorest performing of all. As a result of low-outlet-to-inlet area ratio, increased flow obstruction and increased flow recirculation within the model, the performance measures to be very low and there is a lot of scope for improvement.

The Nusselt numbers calculated using the correlation from the literature hold good in the assumed fully developed flow regions within the HS ducts. Relationship between the calculated Nusselt numbers and the HS temperatures are also indicative of the pertinence of the Nusselt number to the rate of convective heat transfer in a region.

One also needs to consider that the RD model adopted for this study is a very simple model, devoid of a number of minute geometrical details. Furthermore, to mock actual RDs as close as possible, one would also need to include the ventilation fans within the RD, this would introduce more challenges, but would provide more validity to the study. As observed in the experimental tests, acoustical noise generation from these designs is also a possibility and could also be beneficial to investigate in future studies. To conclude with, it must be noted that there exists a dearth of information regarding various practical aspects for the designs to be accepted for commercial use and further investigations are necessary.

Bibliography

[1] X. Li, A. Gani, R. Salleh, and O. Zakaria, “The future of mobile wireless communication networks,” in *2009 International Conference on Communication Software and Networks*, 2009, pp. 554–557.

[2] “Ericsson annual mobility report.” [Online]. Available: https://www.ericsson.com/en/reports-and-papers/mobility-report

[3] K. G. Eze, M. N. Sadiku, and S. M. Musa, “Poiseuille and his law,” *International Journal of Scientific Engineering and Technology*, vol. 7, no. 7, pp. 62–64, 2018.

[4] T. Barnett, S. Jain, U. Andra, and T. Khurana, “Cisco visual networking index (vni) complete forecast update, 2017–2022,” *Americas/EMEAR Cisco Knowledge Network (CKN) Presentation*, 2018.

[5] C. Lange, D. Kosiankowski, R. Weidmann, and A. Gladisch, “Energy consumption of telecommunication networks and related improvement options,” *IEEE Journal of selected topics in quantum electronics*, vol. 17, no. 2, pp. 285–295, 2010.

[6] Telecommunication network diagrams. [Online]. Available: https://www.conceptdraw.com/solution-park/computer-networks-telecommunication

[7] “Under the hood of new multi-band remote radios.” [Online]. Available: https://www.ericsson.com/en/blog/2022/6/under-the-hood-of-new-multi-band-radios

[8] A. Untaroiu, C. Liu, P. J. Migliorini, H. G. Wood, and C. D. Untaroiu, “Hole-Pattern Seals Performance Evaluation Using Computational Fluid Dynamics and Design of Experiment Techniques,” *Journal of Engineering for Gas Turbines and Power*, vol. 136, no. 10, 05 2014, 102501.

[9] K. K. Nielsen, K. Jønck, and H. Underbakke, “Hole-Pattern and Honeycomb Seal Rotordynamic Forces: Validation of CFD-Based Prediction Techniques,” *Journal of Engineering for Gas Turbines and Power*, vol. 134, no. 12, 10 2012, 122505.

[10] R. Boukhanouf and A. Haddad, “A cfd analysis of an electronics cooling enclosure for application in telecommunication systems,” *Applied Thermal Engineering*, vol. 30, no. 16, pp. 2426–2434, 2010, selected Papers from the 12th Conference on Process Integration, Modelling and Optimisation for Energy Saving and Pollution Reduction.

[11] C. W. Leung and H. Kang, “Laminar convection of horizontal and vertical simulated printed-circuit board assemblies,” *Experimental Heat Transfer*, vol. 10, no. 1, pp. 39–49, 1997.

[12] G. R. C. NASA. Bernoulli’s equation. [Online]. Available: https://wright.nasa.gov/airplane/bern.html

[13] R. Eymard, T. Gallouët, and R. Herbin, “Finite volume methods,” in *Solution of Equation in n (Part 3), Techniques of Scientific Computing (Part 3)*, ser. Handbook of Numerical Analysis. Elsevier, 2000, vol. 7, pp. 713–1018. [Online]. Available: https://www.sciencedirect.com/science/article/pii/S1570865900070058

[14] G. Batchelor, *An introduction to fluid dynamics.* Cambridge University Press, 1967, p. 750.

[15] M. F.R., “Two equation eddy-viscosity turbulence models for engineering applications,” *AIAA Journal*, vol. 32, no. 8, pp. 1598–1605, 1994.

[16] E. Toolbox. Fluid flow - hydraulic diameter. [Online]. Available: https://www.engineeringtoolbox.com/hydraulic-equivalent-diameter-d_458.html

[17] B. Zohuri, *Forced Convection Heat Transfer.* Cham: Springer International Publishing, 2017, pp. 323–345. [Online]. Available: https://doi.org/10.1007/978-3-319-53829-7_9

[18] F. P. Incropera, D. P. DeWitt, T. L. Bergman, A. S. Lavine *et al.*, *Fundamentals of heat and mass transfer.* Wiley New York, 1996, vol. 6, p. 371.

[19] J. Backhurst, J. Coulson, J. Harker, and J. Richardson, “Chemical engineering volume 1: Fluid flow, heat transfer and mass transfer,” 1999.

[20] W. H. McAdams, *Heat transmission.* Mcgraw-Hill, 1954.

[21] J. Pftizner, “Poiseuille and his law,” *Anaesthesia*, vol. 31, no. 2, pp. 273–275, 1976.

[22] B. Encyclopaedia. Louver. [Online]. Available: https://www.britannica.com/technology/louver

[23] B. Andersson, R. Andersson, L. Håkansson, M. Mortensen, R. Sudiyo, and B. Van Wachem, *Computational fluid dynamics for engineers.* Cambridge university press, 2011, pp. 37–38.

DEPARTMENT OF SOME SUBJECT OR TECHNOLOGY
CHALMERS UNIVERSITY OF TECHNOLOGY
Gothenburg, Sweden
www.chalmers.se